Coherent Control in Nanolithography: Rydberg Atoms†

Nam A. Nguyen, Bijoy K. Dey,‡ Moshe Shapiro,§ and Paul Brumer*,||

Chemical Physics Theory Group, Department of Chemistry, University of Toronto, Toronto, Ontario, M5S 3H6, Canada

Received: January 20, 2004; In Final Form: April 27, 2004

A technique based on coherent control for the optical manipulation of deposition patterns in nanofabrication with neutral atomic beams is described. The theory, optical nanolithography with bichromatic fields, is then applied to the deposition of rubidium Rydberg atoms on surfaces. Controllable nonperiodic patterns and deposition lines are shown to be possible due to interference contributions to the induced polarizability.

I. Introduction

Traditional photolithography, the mainstream technique for fabricating integral circuits in the microelectronics industry, comprises two steps: patterning of a resist mask and etching of the unmasked regions. During the past three decades the size of integral circuits has decreased considerably, from the micrometer regime to ∼100 nm obtained routinely today. This rate of miniaturization is, however, expected to slow when the inherent physical limitations due to atomic size of the substrate and the diffraction limits of the light sources are reached.

Currently, several alternative techniques are being proposed and developed.[1] One possible approach uses neutral atoms or molecules as a material source and coherent light as a focusing lens;[2−10] i.e., the roles of the light source and the mask are reversed with respect to the traditional photolithographic process. This technique has been made possible by recent advances in laser technology. In contrast with the traditional two-step approach, it is direct write; that is, the need to remove the unmasked region is eliminated, causing less damage to the surface.

Manipulating matter beams with light relies on the fact that light carries momentum, so that a slowly moving atom, in collision with a photon, gets deflected and/or focused. This makes possible the creation of various atom-optical elements, such as lenses,[11−13] lens arrays,[14,15] mirrors,[16−19] beam splitters,[20−22] and waveguides.[23,24] There are two types of forces at work: radiation pressure and the optical dipole force. The latter, acting as confining mechanism, was first considered by Askar'yan[26] in connection with plasmas and neutral atoms. The possibility of trapping atoms with this force was then explored by Letokhov[27] who suggested that atoms might be one-dimensionally confined at the nodes or antinodes of a standing wave tuned above (blue-detuned) or below (red-detuned) the atomic transition frequency. Ashkin[28] demonstrated the trapping of micron-sized particles in a laser light based on the action of the dipole force and later suggested[29] a scheme for three-dimensional neutral atom traps. The dipole force on neutral atoms was also demonstrated by Bjorkholm et al.[11] by focusing an atomic beam using laser light. Chu et al.[30] exploited this force to realize the first optical trap for neutral atoms. In the early 1990s optical dipole forces began to attract increasing interest (see refs 31 and 32), not only for atom trapping but also in the emerging field of atom optics, including nanolithography. Recently, efforts have been made to extend nanolithigraphy to include molecules.[33−35]

In atomic nanofabrication, the topic of this paper, one affects the center of mass motion using the dipole interaction between the atoms and a spatially nonuniform electric field, leading to the confinement of the atoms in regions of space whose size is only a fraction of the optical wavelength. A periodic array of such dipole force causes an atomic beam to form a periodic pattern on a substrate. The advantage of atomic nanofabrication is that neutral atomic beams are simple and inexpensive sources of particles with de Broglie wavelengths < 1 Å. The trajectories of neutral atoms are unaffected by uniform electric or magnetic fields, and the long-range interparticle forces between neutral atoms are small. Also, neutral atoms have laser-accessible internal structures that permit laser cooling,[25] to enhance the flux and collimation of atomic beams.

Almost all of the work done thus far in optically induced atomic nanolithography has produced deposition patterns consisting of periodically repeated parallel lines or an array of ordered atomic dots on a substrate.[2−10] Recently,[41] we suggested a way of overcoming this limitation in order to produce controlled nonperiodic patterns by using the bichromatic coherent control scenario. In general, coherent control affects the outcome of a chemical and physical events by manipulating quantum interferences between different excitation pathways that lead to the same state (for reviews, see refs 37−39). In particular, using such interferences has proven effective in controlling molecular (and atomic) polarizabilities and, by extension, refractive indices,[40] resulting also in the control of nanoscale deposition patterns obtained when molecules (such as N_2[41]) traverse strong electromagnetic fields. In this paper we further explore the ability to produce aperiodic patterns whose structure can be manipulated by altering the parameters of the incident electric fields. Further, we do so with Rydberg atoms, whose large polarizability allows the use of relatively low intensity fields.

The paper is organized as follows. Section II presents the theory behind the coherent control of atomic and molecular

† Part of the special issue "Richard Bersohn Memorial Issue".

* Corresponding author.

‡ Current Address: Department of Chemistry, McMaster University, Hamilton, Ontario, L8S 4M1, Canada.

§ Permanent address: Department of Chemical Physics, The Weizmann Institute of Science, Rehovot, 76100, Israel, and Departments of Chemistry and Physics, University of British Columbia, Vancouver, V6T 1Z1, Canada.

|| Also, Center for Quantum Information and Quantum Control, University of Toronto.

10.1021/jp040035b CCC: $27.50
Published on Web 07/13/2004

dipolar light-induced potentials using bichromatic fields. Section III provides the computational methodology used in calculating the light-induced potential and the trajectories of atoms traversing multicolored electromagnetic fields. Results of the deposition patterns for rubidium atoms in intermediate and high Rydberg states thus obtained are presented in section IV. Conclusions are drawn in section V.

II. Atomic Deposition via Bichromatic Control

Consider an atomic system in a superposition state interacting with a bichromatic electromagnetic field that runs parallel to a surface upon which the atoms will be deposited. The entire system is governed by the light-plus-matter Hamiltonian, given in the dipole approximation by

$$H = K(\mathbf{r}_{cm}) + H_{el}(\mathbf{r}_{el}) - \boldsymbol{\mu}(\mathbf{r})\cdot\mathbf{E}(\mathbf{r}_{cm}, t) \quad (1)$$

where $\mathbf{r}_{cm}$ is the atomic center-of-mass coordinate with associated kinetic energy operator, $K(\mathbf{r}_{cm})$. The vector $\mathbf{r}_{el}$ is the internal (for atoms this is the electronic) coordinate, with $H_{el}(\mathbf{r}_{el})$ denoting the matter Hamiltonian. We denote $\mathbf{r} \equiv \{\mathbf{r}_{el},\mathbf{r}_{cm}\}$ with $-\boldsymbol{\mu}(\mathbf{r})\cdot\mathbf{E}(\mathbf{r}_{cm}, t)$ as the light−matter interaction in the dipole approximation. The term $\boldsymbol{\mu}(\mathbf{r})$ represents the electric-dipole operator, and $\mathbf{E}(\mathbf{r}_{cm}, t)$ is the electric field at the atom center-of-mass.

With x denoting a coordinate parallel to the deposition surface, we assume a bichromatic standing wave with electric field of the form

$$\mathbf{E}(x, t) = \mathbf{E}_1(x, t) + \mathbf{E}_2(x, t) \quad (2)$$

where each term is the sum of two counter-propagating CW fields:

$$\mathbf{E}_i(x, t) = \hat{\boldsymbol{\eta}}_i \frac{E_i^{(0)}}{2} \cos(k_i x + \phi_i)[\exp(-i\omega_i^F t) + c.c.] \quad i = 1, 2 \quad (3)$$

where $\hat{\boldsymbol{\eta}}_i$ denotes the polarization direction of the ith field. Here the two polarizations are taken to be parallel to one another and perpendicular to x, and aligned, as depicted in Figure 1, along the laboratory frame z axis which is taken to be perpendicular to the surface. We denote the spatial part of the ith standing wave field by $F_i(x) \equiv \cos(k_i x + \phi_i)$, and the relative phase between the two fields by $\phi_F \equiv \phi_2 - \phi_1$.

We choose the initial atomic state to be a superposition state:

$$\Psi_s(t) = b_1\Phi_1 \exp(-i\omega_1 t) + b_2\Phi_2 \exp(-i\omega_2 t) \quad (4)$$

where Φ_i and $\hbar\omega_i$ are, respectively, two eigenfunctions and eigenvalues of $H_{el}(\mathbf{r}_{el})$,

$$H_{el}(\mathbf{r}_{el})\Phi_i = \hbar\omega_i\Phi_i, \quad i = 1, 2 \quad (5)$$

Given eq 4, the frequencies of the CW fields are chosen such that

$$\omega_1^F - \omega_2^F \equiv \omega_{1,2}^F \approx \omega_{2,1} \equiv \omega_2 - \omega_1 \quad (6)$$

Basically, the light field affects the trajectories of the atomic center-of-mass motion through V_{LIP}, the "light-induced potential", which results from the interaction of the electric field with an atomic dipole moment $\langle\boldsymbol{\mu}_{ind}\rangle$ that it induces. That is,

$$V_{LIP} = -\langle\boldsymbol{\mu}_{ind}\rangle\cdot\mathbf{E}(\mathbf{r}_{cm}, t) \quad (7)$$

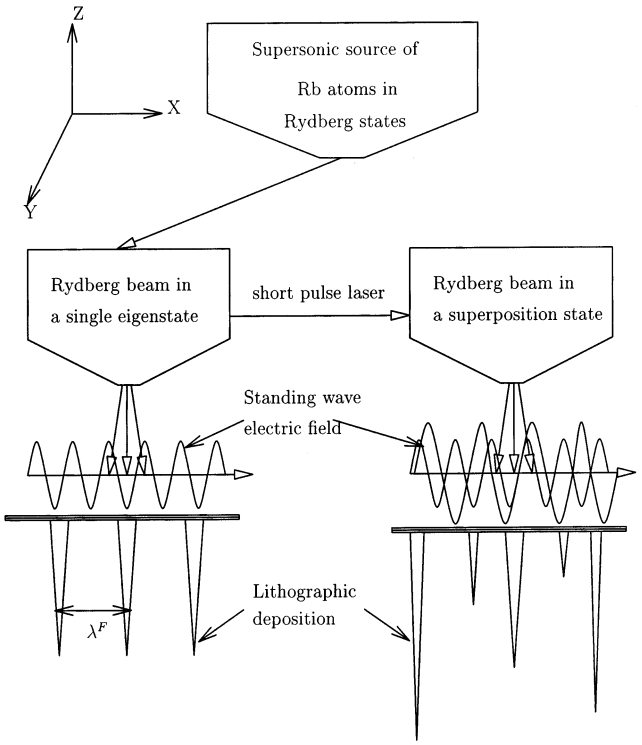

Figure 1. Schematic representation of the lithographic experiment for the Rb atom beam in a Rydberg state. The schematic on the left-hand side shows periodic deposition from a single Rydberg state. The schematic on the right-hand side shows controlled deposition from a superposition of Rydberg states.

Altering this potential (through interference or other means) allows for the manipulation of the resultant deposition pattern.

A. Controlling the Light-Induced Dipole. We can separate the center-of-mass motion from the much faster electronic motion using the adiabatic Born−Oppenheimer approximation to obtain a Schrödinger equation in the space of the electrons that is parametrically dependent on $\mathbf{r}_{cm}$:

$$i\hbar\frac{\partial}{\partial t}\Psi_{el}(\mathbf{r}_{el}, t|\mathbf{r}_{cm}) = [H_{el}(\mathbf{r}_{el}) - \boldsymbol{\mu}(\mathbf{r}_{el}|\mathbf{r}_{cm})\cdot\mathbf{E}(\mathbf{r}_{cm}, t)]\Psi_{el}(\mathbf{r}_{el}, t|\mathbf{r}_{cm}) \quad (8)$$

For weak fields, first-order time-dependent perturbation theory can be used, according to which the solution of eq 8 is given by

$$\Psi_{el}(\mathbf{r}_{el}, t|\mathbf{r}_{cm}) = \Psi_s(t) + \sum_{e>2} c_e(t)\Phi_e(\mathbf{r}_{el}) \exp(-i\omega_e t) \quad (9)$$

The subscript e, $e > 2$, refers to the excited states of $H_{el}(\mathbf{r}_{el})$ with respect to the initial superposition state $\Psi_s(t)$. Below, we are concerned with center-of-mass motion along one direction. Hence, we replace $\mathbf{r}_{cm}$ by the coordinate x. The coefficients $c_e(t)$ in eq 9 are given by

$$c_e(t) = \frac{1}{\hbar}\sum_{i=1}^{2} b_i \sum_{k=1}^{2} \mu_{e,i}^{(k)} E_k^{(0)} F_k(x)/ 2\left\{\frac{\exp[i(\omega_{e,i} - \omega_k^F)t] - 1}{\omega_{e,i} - \omega_k^F} + \frac{\exp[i(\omega_{e,i} + \omega_k^F)t] - 1}{\omega_{e,i} + \omega_k^F}\right\} \quad (10)$$

where $\mu_{e,i}^{(k)} = \langle\Phi_e|\hat{\boldsymbol{\eta}}_k\cdot\boldsymbol{\mu}|\Phi_i\rangle$ are the transition dipole moments. To avoid divergences on resonance, i.e., when $\omega_{e,i} = \omega_k^F$, we

add below to the denominators of the final expression factors of $-i\Gamma_e/2$ where Γ_e are experimentally determined line widths.

It follows from eq 10 that the probability $|c_e(t)|^2$ of excitation from the initial superposition state $\Psi_s(t)$ to a state Φ_e arises through three different terms: (1) the excitation of Φ_e, having started from Φ_1, with probability proportional to $|b_1|^2$; (2) the excitation of Φ_e, having started from Φ_2, with probability proportional to $|b_2|^2$; and (3) the interference between these two pathways, which is proportional to $2R_e\{b_1^*b_2\} = 2|b_1b_2|\cos(\phi_M)$, where ϕ_M is the (experimentally controllable) relative phase between b_1 and b_2. Note that this interference term owes its existence to the presence of both a bichromatic field and a coherent superposition state, to which the two colors of the field are coupled.

Using eq 9 we can write an expression for the expectation value of the dipole moment:

$$\langle\boldsymbol{\mu}\rangle = b_2^*b_1\mu_{2,1}\exp(i\omega_{2,1}t) + \text{c.c.} + \sum_{i'=1}^{2}\sum_{e>2}c_e(t)b_{i'}^*\boldsymbol{\mu}_{i',e}\exp(i\omega_{i',e}t) + \text{c.c.} + \sum_{e'>2}\sum_{e>2}c_{e'}^*(t)c_e(t)\boldsymbol{\mu}_{e',e}\exp(i\omega_{e',e}t) \quad (11)$$

where "c.c." denotes the complex conjugate of the term that precedes it.

The dipole moment is seen to be a sum of a "field independent" and a "field induced" terms

$$\langle\boldsymbol{\mu}\rangle = \langle\Psi_{el}|\mu|\Psi_{el}\rangle = \langle\mu_1(t)\rangle + \langle\mu_{ind}(x,t)\rangle \quad (12)$$

where the field independent term is given by

$$\langle\boldsymbol{\mu}_1(t)\rangle = b_2^*b_1\mu_{2,1}\exp(i\omega_{2,1}t) + \text{c.c.} \quad (13)$$

The field-induced term $\langle\boldsymbol{\mu}_{ind}(x,t)\rangle$ depends on $c_e(t)$ [eq 10] and, after neglecting the quadratic terms in accord with the weak field assumption, is given by

$$\langle\boldsymbol{\mu}_{ind}(x,t)\rangle = \frac{1}{2\hbar}\sum_{i'=1}^{2}\sum_{i=1}^{2}\sum_{k=1}^{2}E_k^{(0)}F_k(x)\sum_{e>2}b_ib_{i'}^*\boldsymbol{\mu}_{i',e}\mu_{e,i}^{(k)}\left\{\frac{\exp[i(\omega_{i',i}-\omega_k^F)t]-\exp(i\omega_{i',e}t)}{\omega_{e,i}-\omega_k^F} + \frac{\exp[i(\omega_{i',i}+\omega_k^F)t]-\exp(i\omega_{i',e}t)}{\omega_{e,i}+\omega_k^F}\right\} + \text{c.c.} \quad (14)$$

Thus, the induced dipole moment can be controlled by properly choosing ϕ_F, ϕ_M, or $|b_1/b_2|$. Below we show that these parameters are useful in controlling the deposition pattern on a surface. In doing so we focus, as a specific example, on the case of hydrogenic-like wave functions $\langle\mathbf{r}_{el}|n,l,m\rangle$, where n, l, m denote the principal, angular momentum, and magnetic quantum numbers, respectively. In particular, if Φ_1 is described by the n_1, l_1, m_1 quantum numbers, then we choose n_2, l_2, m_2 of Φ_2 as $n_2 = n_1$, $l_2 = l_1 + 2$, and $m_2 = m_1$.

B. The Light-Induced Potential. The translational motion of the center-of-mass of the atoms is governed by the spatially inhomogeneous induced dipole which gives rise to a "light-induced" potential $V_{LIP}(x,t)$. This potential, given by

$$V_{LIP}(x,t) = -\langle\boldsymbol{\mu}\rangle\cdot\mathbf{E}(x,t) \quad (15)$$

has two components,

$$V_{LIP}(x,t) = V^{(1)}(x,t) + V^{(2)}(x,t) \quad (16)$$

where $V^{(1)}(x,t)$ is linear in the electric field and arises from the field-independent dipole of eq 13, and $V^{(2)}(x,t)$ is quadratic in the field and arises from the field-induced dipole of eq 14. That is,

$$V^{(1)}(x,t) = -\langle\boldsymbol{\mu}_z(t)\rangle\sum_{\ell}\mathbf{E}_{\ell}(x,t)$$
$$V^{(2)}(x,t) = -\langle\boldsymbol{\mu}_{ind}(x,t)\rangle\sum_{\ell}\mathbf{E}_{\ell}(x,t) \quad (17)$$

Inserting eq 14 into eq 17 gives the quadratic part of the light-induced potential as

$$V^{(2)}(x,t) = \frac{-1}{4\hbar}\sum_{k=1}^{2}\sum_{\ell=1}^{2}E_k^{(0)}F_k(x)E_{\ell}^{(0)}F_{\ell}(x)\sum_{i=1}^{2}\sum_{i'=1}^{2}\sum_{n_el_em_e}b_i^*b_{i'}\mu_{i',e}^{(\ell)}\mu_{e,i}^{(k)}\left\{\frac{\exp[i(\omega_{i',i}-\omega_k^F-\omega_{\ell}^F)t]-\exp[i(\omega_{i',e}-\omega_{\ell}^F)t]}{\omega_{e,i}-\omega_k^F} + \frac{\exp[i(\omega_{i',i}+\omega_{k,\ell}^F)t]-\exp[i(\omega_{i',e}-\omega_{\ell}^F)t]}{\omega_{e,i}+\omega_k^F} + \frac{\exp[i(\omega_{i',i}-\omega_{k,\ell}^F)t]-\exp[i(\omega_{i',e}+\omega_{\ell}^F)t]}{\omega_{e,i}-\omega_k^F} + \frac{\exp[i(\omega_{i',i}+\omega_k^F+\omega_{\ell}^F)t]-\exp[i(\omega_{i',e}+\omega_{\ell}^F)t]}{\omega_{e,i}+\omega_k^F}\right\} + \text{c.c.} \quad (18)$$

The potential $V^{(2)}(x,t)$ can be written as a sum of two terms

$$V^{(2)}(x,t) = V^{non}(x,t) + V^{int}(x,t) \quad (19)$$

where $V^{non}(x,t)$, the non-interference term, is obtained from the $i = i'$ part of $V^{(2)}(x,t)$ of eq 19 and $V^{int}(x,t)$, the interference term, is a result of the $i \neq i'$ contribution to $V^{(2)}(x,t)$.

Consider then these two contributions. The first is given by

$$V^{non}(x,t) = \frac{-1}{4\hbar}\sum_{k=1}^{2}\sum_{\ell=1}^{2}E_k^{(0)}F_k(x)E_{\ell}^{(0)}F_{\ell}(x)\sum_{i=1}^{2}\sum_{n_el_em_e}|b_i|^2\mu_{i,e}^{(\ell)}\mu_{e,i}^{(k)}\left\{\frac{\exp[-i(\omega_k^F+\omega_{\ell}^F)t]-\exp[i(\omega_{i,e}-\omega_{\ell}^F)t]}{\omega_{e,i}-\omega_k^F} + \frac{\exp[i\omega_{k,\ell}^Ft]-\exp[i(\omega_{i,e}-\omega_{\ell}^F)t]}{\omega_{e,i}+\omega_k^F} + \frac{\exp[-i\omega_{k,\ell}^Ft]-\exp[i(\omega_{i,e}+\omega_{\ell}^F)t]}{\omega_{e,i}-\omega_k^F} + \frac{\exp[i(\omega_k^F+\omega_{\ell}^F)t]-\exp[i(\omega_{i,e}+\omega_{\ell}^F)t]}{\omega_{e,i}+\omega_k^F}\right\} + \text{c.c.} \quad (20)$$

Because the time of passage of the atoms through the fields' region is much larger than the optical periods of the fields, we can, in thin samples, ignore the highly oscillatory terms in the above equations and retain only the slowly oscillating terms. Hence, with the largest contribution coming from the $k = \not{}$ terms, we have

$$V^{\mathrm{non}}(x, \omega_1^F, \omega_2^F) \approx \frac{-1}{2\hbar}\sum_{k=1}^{2}(E_k^{(0)}F_k(x))^2\sum_{i=1}^{2}\sum_{n_e l_e m_e}|b_i|^2\left[\frac{|\mu_{i,e}^{(k)}|^2}{\omega_{e,i}+\omega_k^F}+\frac{|\mu_{i,e}^{(k)}|^2}{\omega_{e,i}-\omega_k^F}\right] \quad (21)$$

For $V^{\mathrm{int}}(x, t)$, the interference-induced term, derived from the $i \neq i'$ terms, we obtain that

$$\begin{aligned}V^{\mathrm{int}}(x,t) = \frac{-1}{4\hbar}\sum_{k=1}^{2}\sum_{\not{}=1}^{2}E_k^{(0)}F_k(x)E_{\not{}}^{(0)}F_{\not{}}(x)\sum_{n_e l_e m_e}\Bigg[b_1 b_2^*\mu_{2,e}^{(\not{})}\mu_{e,1}^{(k)}\times \\ \Bigg\{\frac{\exp[i(\omega_{2,1}-\omega_k^F-\omega_{\not{}}^F)t]-\exp[i(\omega_{2,e}-\omega_{\not{}}^F)t]}{\omega_{e,1}-\omega_k^F}+ \\ \frac{\exp[i(\omega_{2,1}+\omega_{k,\not{}}^F)t]-\exp[i(\omega_{2,e}-\omega_{\not{}}^F)t]}{\omega_{e,1}+\omega_k^F}+ \\ \frac{\exp[i(\omega_{2,1}-\omega_{k,\not{}}^F)t]-\exp[i(\omega_{2,e}+\omega_{\not{}}^F)t]}{\omega_{e,1}-\omega_k^F}+ \\ \frac{\exp[i(\omega_{2,1}+\omega_k^F+\omega_{\not{}}^F)t]-\exp[i(\omega_{2,e}+\omega_{\not{}}^F)t]}{\omega_{e,1}+\omega_k^F}\Bigg\}+ \\ b_2 b_1^*\mu_{1,e}^{(\not{})}\mu_{e,2}^{(k)}\times \\ \Bigg\{\frac{\exp[-i(\omega_{2,1}+\omega_k^F+\omega_{\not{}}^F)t]-\exp[i(\omega_{1,e}-\omega_{\not{}}^F)t]}{\omega_{e,2}-\omega_k^F}+ \\ \frac{\exp[-i(\omega_{2,1}-\omega_{k,\not{}}^F)t]-\exp[i(\omega_{1,e}-\omega_{\not{}}^F)t]}{\omega_{e,2}+\omega_k^F}+ \\ \frac{\exp[-i(\omega_{2,1}+\omega_{k,\not{}}^F)t]-\exp[i(\omega_{1,e}+\omega_{\not{}}^F)t]}{\omega_{e,2}-\omega_k^F}+ \\ \frac{\exp[-i(\omega_{2,1}-\omega_k^F-\omega_{\not{}}^F)t]-\exp[i(\omega_{1,e}+\omega_{\not{}}^F)t]}{\omega_{e,2}+\omega_k^F}\Bigg\}+\mathrm{c.c.}\Bigg]\end{aligned} \quad (22)$$

Eliminating the most rapidly oscillating terms we obtain

$$\begin{aligned}V^{\mathrm{int}}(x,t) \approx \frac{-1}{4\hbar}\sum_{k=1}^{2}\sum_{\not{}=1}^{2}E_k^{(0)}F_k(x)E_{\not{}}^{(0)}F_{\not{}}(x)\sum_{n_e l_e m_e} \\ \Bigg[b_1 b_2^*\mu_{2,e}^{(\not{})}\mu_{e,1}^{(k)}\Bigg\{\frac{\exp[i(\omega_{2,1}+\omega_{k,\not{}}^F)t]}{\omega_{e,1}+\omega_k^F}+\frac{\exp[i(\omega_{2,1}-\omega_{k,\not{}}^F)t]}{\omega_{e,1}-\omega_k^F}\Bigg\}+ \\ b_2 b_1^*\mu_{1,e}^{(\not{})}\mu_{e,2}^{(k)}\Bigg\{\frac{\exp[-i(\omega_{2,1}-\omega_{k,\not{}}^F)t]}{\omega_{e,2}+\omega_k^F}+ \\ \frac{\exp[-i(\omega_{2,1}+\omega_{k,\not{}}^F)t]}{\omega_{e,2}-\omega_k^F}\Bigg\}+\mathrm{c.c.}\Bigg]\end{aligned} \quad (23)$$

Retaining only the least oscillatory terms, satisfying the $\omega_{1,2}^F \approx \omega_{2,1}$ condition of eq 6, we finally have that

$$V^{\mathrm{int}}(x) \approx \frac{-1}{2\hbar}E_1^{(0)}F_1(x)E_2^{(0)}F_2(x)\sum_{n_e l_e m_e}b_1 b_2^*\left\{\frac{\mu_{2,e}^{(1)}\mu_{e,1}^{(2)}}{\omega_{e,1}+\omega_2^F}+\frac{\mu_{2,e}^{(2)}\mu_{e,1}^{(1)}}{\omega_{e,1}-\omega_1^F}\right\}+\mathrm{c.c.} \quad (24)$$

The results of eqs 21 and 24 for the non-interference and interference-induced LIP can be expressed in terms of two polarizability tensors $\underline{\underline{\chi}}$

$$\begin{aligned}V^{\mathrm{non}}(x) &= \sum_{k=1,2}-E_k^{(0)}\boldsymbol{\eta}_k\underline{\underline{\chi}}_k^{\mathrm{non}}(x)\,\boldsymbol{\eta}_k E_k^{(0)} \\ V^{\mathrm{int}}(x) &= -E_1^{(0)}\boldsymbol{\eta}_1\,\underline{\underline{\chi}}^{\mathrm{int}}(x)\,\boldsymbol{\eta}_2 E_2^{(0)}\end{aligned} \quad (25)$$

where $\underline{\underline{\chi}}_k^{\mathrm{non}}(x)$ and $\underline{\underline{\chi}}^{\mathrm{int}}(x)$ are defined as

$$\underline{\underline{\chi}}_k^{\mathrm{non}}(x) = \frac{1}{2\hbar}(F_k(x))^2\sum_{i=1}^{2}\sum_{n_e l_e m_e}|b_i|^2\boldsymbol{\mu}_{i,\mathrm{e}}\otimes\boldsymbol{\mu}_{e,i}\left[\frac{1}{\omega_{e,i}+\omega_k^F-i\Gamma_e/2}+\frac{1}{\omega_{e,i}-\omega_k^F-i\Gamma_e/2}\right] \quad (26)$$

and

$$\begin{aligned}\underline{\underline{\chi}}^{\mathrm{int}}(x) = \frac{1}{2\hbar}F_1(x)F_2(x)\sum_{n_e l_e m_e}b_1 b_2^*\Bigg[\frac{\boldsymbol{\mu}_{2,e}\otimes\boldsymbol{\mu}_{e,1}}{\omega_{e,1}+\omega_2^F-i\Gamma_e/2}+ \\ \frac{\boldsymbol{\mu}_{e,1}\otimes\boldsymbol{\mu}_{2,e}}{\omega_{e,1}-\omega_1^F-i\Gamma_e/2}\Bigg]+b_1^* b_2\Bigg[\frac{\boldsymbol{\mu}_{e,2}\otimes\boldsymbol{\mu}_{1,e}}{\omega_{e,1}+\omega_2^F-i\Gamma_e/2}+ \\ \frac{\boldsymbol{\mu}_{1,e}\otimes\boldsymbol{\mu}_{e,2}}{\omega_{e,1}-\omega_1^F-i\Gamma_e/2}\Bigg]\end{aligned} \quad (27)$$

where $\otimes$ signifies the outer product between two vectors (e.g., $(\mathbf{a}\otimes\mathbf{b})_{x,y} \equiv \mathbf{a}_x\mathbf{b}_y$), and where phenomenological widths Γ_e have been added to the levels to account for spontaneous emission and other line-broadening mechanisms.

Note that $V^{(2)}(x)$ is the only potential included in the calculations below since $\mu_{1,2}$, and hence $V^{(1)}(x, t)$ is zero for the choice of $l_2 = l_1 + 2$, since Φ_1 and Φ_2 are of the same parity. Note that for Φ_1 and Φ_2 of opposite parity (e.g., $l_2 = l_1 + 1$), $V^{\mathrm{int}} = 0$, and hence the desired interference term vanishes. The potential $V^{(2)}(x)$ calculated using eqs 21 and 24 consists of a series of wells aligned along the x direction, of varying depths and periodicity. The structure of the potential can be experimentally controlled by varying any or all of the following: (a) the frequencies of the two standing wave fields, ω_1^F and ω_2^F, (b) the field strengths ratio, $E_1^{(0)}/E_2^{(0)}$, (c) the relative phase between the two standing waves, ϕ_F, (d) the relative phase of the initial coefficients of the superposition state, ϕ_M, and/or (e) the ratio $|b_1/b_2|$.

III. Computational Methodology

The treatment above provides a general theory for the coherent control of atomic and molecular trajectories using two

standing wave fields. In this section we apply the approach to Rydberg atoms, whose polarizabilities are, conveniently, very large. Additional studies on non-Rydberg atoms are underway.[43]

Rydberg atoms, such as those studied in this paper, can be treated as quasi-hydrogenic, with each Rydberg state approximated as a one-electron orbital. Specific details of the polarizability contributions are given in this section. Rubidium has been chosen as a prototype, but the calculations can be generalized to other alkali metals. We also present details on the numerical calculation of the deposition patterns.

A. Polarizability Calculation. The Rydberg state of the Rb atom described by principal quantum number n and angular momentum quantum number l has an energy approximated by

$$E_{n,l} = -\frac{Ry(\infty)(1 + m_e/M_{nu})^{-1}}{(n - \delta_l)^2} \tag{28}$$

where $Ry(\infty)$ is the Rydberg constant for the Rb atom calculated from the Rydberg constant assuming infinite mass of the nucleus and m_e and M_{nu} are the mass of electron and the Rubidium nucleus respectively.[44,45] Here δ_l is the quantum defect which describes deviations of the Rydberg series from atomic hydrogen for the state with quantum number l. For Rb, $\delta_s = 3.135$, $\delta_p = 2.65$, $\delta_d = 1.34$ $\delta_f = 0.033$;[46] states of higher l have negligible quantum defect and behave like pure hydrogenic states.

To evaluate the polarizability contributions we first calculate the transition dipole moments. Applying quantum defect theory gives analytic expressions for the transition dipole moments:[44]

$$\mu_{e,i}^{(z)} = e_{el}\langle n_e l_e|\ r\ |nl\rangle\langle l_e m_e|\ \cos\theta\ |lm\rangle \tag{29}$$

where e_{el} is the electronic charge. (Recall that the subscript e indexes the states.) The radial matrix elements $\langle n_e l_e|\ r\ |nl\rangle$ were evaluated analytically using the method developed by Kostelecky and Nieto.[47] Note that in evaluating $\langle n_e l_e|\ r\ |nl\rangle$ the physical quantum numbers n, l, n_e, and l_e are replaced by the corresponding effective quantum numbers n^*, l^*, n_e^*, and l_e^*, which incorporate the proper quantum defect. The quantum defects δ_l and δ_{l_e} in $n^* = n - \delta_l$ and $n_e^* = n_e - \delta_{l_e}$ represent the effective charge created by the core electrons and the nucleus phenomenologically by shifting the eigenvalues away from the hydrogenic values. The effective angular quantum numbers, $l^* = l - \delta_l + I(l)$ and $l_e^* = l_e - \delta_{l_e} + I(l_e)$ ($I(l)$, $I(l_e) = 0, 1, 2$), on the other hand, do not have physical meaning. They were introduced artificially in ref 47 in order to make the expression for the evaluation of transition probabilities analytical.

The angular integral $\langle l_e m_e|\ \cos\theta\ |lm\rangle$ is simplified by using the spherical harmonics

$$\langle l_e m_e|\ \cos\theta\ |lm\rangle = \sqrt{\frac{4\pi}{3}}\langle l_e m_e|\ Y_{10}\ |lm\rangle$$

$$= \sqrt{\frac{4\pi}{3}}\left(\frac{3(2l+1)(2l_e+1)}{4\pi}\right)^{1/2} (-1)^{m_e}\begin{pmatrix} 1 & l & l_e \\ 0 & m & -m_e \end{pmatrix}\begin{pmatrix} 1 & l & l_e \\ 0 & 0 & 0 \end{pmatrix} \tag{30}$$

TABLE 1: Static Polarizabilities (atomic units, i.e., a_0^3) of *n*s States of Rb

	results	
n	calcd.	exptl.[48]
8	0.1126696×10^6	0.1314194×10^6
9	0.3572713×10^6	0.4114472×10^6
10	0.9496947×10^6	0.1078768×10^7
11	0.2217497×10^7	0.2485978×10^7
12	0.4690786×10^7	0.5193317×10^7
13	0.9180168×10^7	0.1004327×10^8
14	0.1687154×10^8	0.1824944×10^8
15	0.2943914×10^8	0.3150063×10^8
16	0.4918174×10^8	0.5208120×10^8
17	0.7921468×10^8	0.8300864×10^8
18	0.1241597×10^9	0.1281894×10^9
19	0.1954441×10^9	0.1925937×10^9

To test the reliability of these expressions we computed the polarizabilities of an eigenstate $|\Phi_i\rangle$ of Rb:

$$\underline{\underline{\chi}}_i(\omega^F) = \frac{1}{\hbar}\sum_e \boldsymbol{\mu}_{i,e} \otimes \boldsymbol{\mu}_{e,i}\left[\frac{1}{\omega_{e,i} + \omega^F - i\Gamma_e/2} + \frac{1}{\omega_{e,i} - \omega^F - i\Gamma_e/2}\right] \tag{31}$$

where i refers to n, l, m and the e sum is over n_e, l_e, and m_e. Specifically, we computed the zz component of the polarizability tensor, given by

$$\chi_{nlm}^{(zz)}(\omega^F) = \frac{e_{el}^2}{\hbar}\sum_{n_e l_e m_e} |\langle n_e l_e|\ r\ |nl\rangle|^2 \frac{4\pi}{3} \frac{3(2l+1)(2l_e+1)}{4\pi}(-1)^{2m_e}\begin{pmatrix} 1 & l & l_e \\ 0 & m & -m_e \end{pmatrix}^2\begin{pmatrix} 1 & l & l_e \\ 0 & 0 & 0 \end{pmatrix}^2 \left[\frac{1}{\omega_{e,i} + \omega^F - i\Gamma_e/2} + \frac{1}{\omega_{e,i} - \omega^F - i\Gamma_e/2}\right] \tag{32}$$

The computed static polarizabilities ($\omega^F = 0$) for different Rydberg states of Rb are shown in Table 1 along with the experimental values;[48] satisfactory agreement for our purposes is seen. The high polarizability values (both static and dynamic) obtained are useful for lithography insofar as one can use relatively weak electric fields for the controlled deposition. Also, Rydberg atoms can be deflected more easily than their ground state counterparts. As a result, we can concentrate the atomic Rydberg beam by deflecting the Rydberg atoms before the deposition process, thus reducing the background noise caused by ground state atoms. To this end we note that controlled deflection of Rydberg molecules, for example, was recently demonstrated experimentally by Softley et al.[49]

Figure 2 depicts the interference contribution to the polarizability at parameters given in the figure caption, and Table 2 gives, as examples, the real parts of the non-interference and interference polarizability contributions for several parameter sets. The non-interference contribution, $\underline{\underline{\chi}}_k^{non}(x)$, is found to be 1 order of magnitude smaller than the interference contribution. Note that the non-interference contribution does not change with ϕ_M, and the range of control over the magnitude of the polarizability is vast.

B. Atomic Density Distribution. Consider, then, a beam of atoms to be deposited on a surface. The motion of the center-

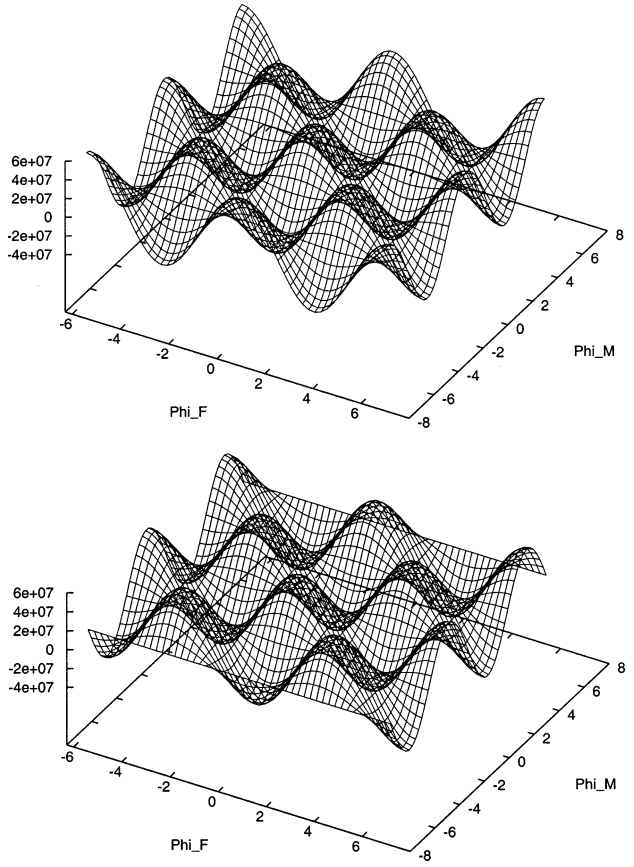

Figure 2. Interference contribution to the polarizability (in a.u.) at $x = 0$, plotted against ϕ_M and ϕ_F for the $\sqrt{0.8}|16, 0, 0\rangle + \sqrt{0.2}|16, 2, 0\rangle$ superposition state. Two SW fields are of intensity $I_1 = 13.3$ W/cm^2 and $I_2 = 132537$ W/cm^2 at wavelengths of $\lambda_1 = 41876$ nm and $\lambda_2 = 115781$ nm. Upper panel is the real part of $\underline{\underline{\chi}}^{\text{int}}(x)$ and the lower one is the imaginary part.

TABLE 2: Contribution of the Non-interference and Interference Dynamic Polarizabilities (atomic units)[a]

ϕ_F	$\text{Re}(\underline{\underline{\chi}}_k^{\text{non}})$	$\text{Re}(\underline{\underline{\chi}}_k^{\text{int}})^b$
0.1282	0.8469×10^7	4.6735×10^7
		2.9380×10^7
		-0.4525×10^7
0.8976	0.5324×10^7	2.9380×10^7
		1.8471×10^7
		-0.2845×10^7
1.6669	-0.8199×10^6	-0.4525×10^7
		-0.2845×10^7
		0.4381×10^6

[a] Parameters given in the caption of Figure 2. [b] Results correspond to $\phi_M = 0.1282$, 0.8976, 1.6669, respectively.

of-mass of each atom is governed by Hamilton's equation of motion:

$$M\frac{\partial}{\partial t}x_i = p_i^x \tag{33}$$

and

$$\frac{\partial}{\partial t}p_i^x = -\frac{\partial}{\partial x}V_{\text{LIP}}(x, t)|_{x_i} \tag{34}$$

where x_i, p_i, and M are the position, momentum, and mass of the ith atom, respectively. The above equations must be solved for the ensemble $\{x_i(t)\}$ of the atomic trajectories, where $x_i(t)$ is the x projection of the position of the ith atom, to obtain the atomic density $\rho(x, t)$. Results are determined from a uniform initial distribution of atoms at time $t = t_{\text{inter}} + (L_{\text{ff}}/v_{\parallel})$, where t_{inter} is the actual atom-field interaction time and L_{ff} is the free-flight distance of the atomic beam.

The computation of the deposition pattern involves the following steps. (1) At $t = 0$, a fixed number of atoms is uniformly distributed over a small nozzle segment $-a\lambda_2 \le x \le a\lambda_2$, where a is a constant and λ_2 is the longest wavelength of the two standing wave fields. This nozzle segment is subdivided into $N - 1$ cells of size $\Delta x = 2a\lambda_2/(N - 1)$, where Δx is chosen sufficiently small so that the force at x_i, which is the gradient of the LIP, remains constant over the cell. (2) Given a time t_0, the LIP is calculated at every point $x_i = -a\lambda_2 + (i - 1)\Delta x$, $(i = 1,2,....,N)$. Hamilton's equations are solved to obtain $v_i^x = p_i^x/M$ at time $t = t_0 + \Delta t$. The Δt time step is chosen small enough to maintain energy conservation. Since there are no forces in the y and z directions, the v_i^y and v_i^z velocity components are constant. Supplementing these values with the v_i^x information obtained from Hamilton's equations gives the atomic positions (x_i, y_i, and z_i) for each atom in the ensemble at time $t = t_0 + \Delta t$. The procedure is repeated until the atom hits the surface (at $z_i = 0$). (3) After all the trajectories have terminated, the density of the atoms on the surface is analyzed by considering a segment of size $-b\lambda_2 \le x \le b\lambda_2$, where $b > a$. The constant b is chosen large enough to include all deposited trajectories. Histograms of the data provide the deposited density.

IV. Numerical Results and Discussion

The general configuration of the nanofabrication experiment is illustrated in Figure 1. We envision using Rb atoms in Rydberg states prepared by an optical excitation from the (5^2S) ground state.[44] After excitation, the Rydberg atoms are mixed with an inert buffer gas and the mixture is supersonically expanded through a nozzle to narrow down the translational velocity distribution.

The average longitudinal velocity of a supersonic source is $v_{\parallel} = \sqrt{2k\gamma T_0/(M_b(\gamma-1))}$, where k is the Boltzmann constant, M_b is the mass of the buffer gas atom, $\gamma = C_p/C_v$ is the specific heat ratio of the buffer gas, and T_0 is the initial temperature. After exiting the nozzle, the supersonic Rb Rydberg atom beam can be collimated by letting it pass through a series of slits.[50] Alternatively, or additionally, the beam can be collimated by cooling the transverse velocity with a transverse laser field[51] to a temperature low enough to ensure no escape from the light-induced potential well. Preparation of the Rb atoms in a *single* Rydberg level can be done by combining optical pumping and "locking".[52]

The LIP experienced by an atom in a single Rydberg state subjected to a single frequency is periodic, leading to deposition patterns consisting of equally spaced peaks. A sample is shown in Figure 3, which displays the trajectories and associated deposition for Rb in the 16s state. As described above, to control the deposition pattern we can prepare an initial superposition of two states using an additional laser pulse.

Coherent modification of the polarizabilities and of the refractive index of atoms and molecules[40] can be achieved with either off-resonant or near-resonant fields. Here, however, because the LIP is governed by a combination of the natural and altered polarizability *and* the external electric fields, a number of conditions must be satisfied to make the control possible.

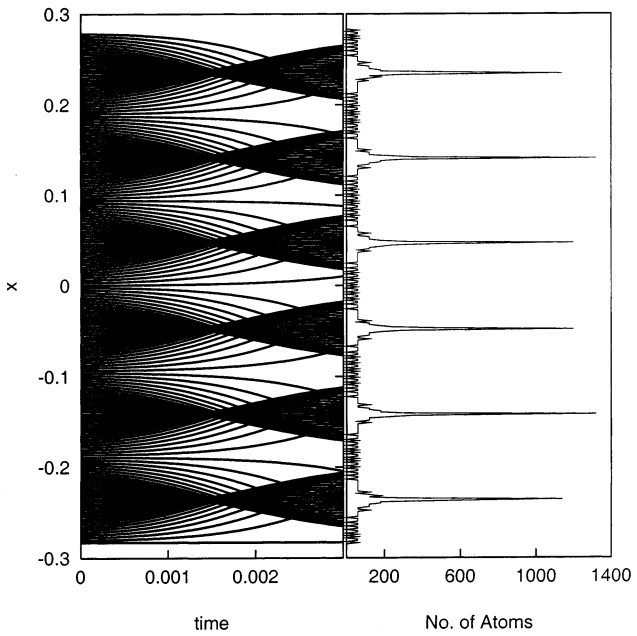

Figure 3. (Left) Atomic trajectories, with time in μs. Note the dark focusing regions. (Right) Number of atoms distributed periodically along x (in μm) at $t_{inter} = 0.0012$ μs. The results correspond to the 16S state of Rb atom where $I = 1.9 \times 10^{13}$ W/cm^2, $\lambda = 188.5$ nm. Deposition plate size = 1319.5 nm and the nozzle width is 565.5 nm. The plate is 0.6 μm away from the nozzle.

Note first, as shown in eq 24, that $V^{int}(x)$ is proportional to the product of the field amplitudes, $E_1^{(0)} E_2^{(0)}$. By contrast, the non-interference contribution, $V^{non}(x)$, [eq 21] is a sum of terms that depends on either $E_1^{(0)^2}$ or on $E_2^{(0)^2}$. Thus, when $E_1^{(0)} \ll E_2^{(0)}$ or $E_1^{(0)} \gg E_2^{(0)}$, the periodicity of $V^{non}(x)$ dominates, leading to a periodic LIP and to the suppression of coherence effects. The resulting deposition pattern will thus be periodic. To break this periodicity and provide control requires that $E_1^{(0)} \approx E_2^{(0)}$.

Second, the frequencies of the electric fields have to be near-resonant with an atomic transition. This follows from eqs 26 and 27, according to which if the fields are far off-resonance then we can approximate all the $\omega_{ej} - \omega_2^F$, ($j = 1, 2$), terms by a common denominator and factor it out of the sums. Further, since in eq 26 $\mu_{je}^{(k)} \mu_{ej}^{(k)}$, ($j = 1, 2$) > 0, whereas in eq 27 $\mu_{1e}^{(1)} \mu_{e2}^{(2)}$ may take any (complex) value depending on ϕ_e, we have that $\sum_{n_e l_e m_e} \mu_{je}^{(k)} \mu_{ej}^{(k)} > \sum_{n_e l_e m_e} \mu_{1e}^{(1)} \mu_{e2}^{(2)}$. Consequently, in this case, the non-interference polarizability contribution would be far bigger than its interference-induced counterpart, resulting in a periodic LIP and a periodic deposition pattern.

By contrast, if the fields are near-resonant then there exists a Φ_e which, due to the $1/(\omega_{ej} - \omega_2^F)$ term, dominates the entire sum, which then reduces to one term. In this case the polarizability depends strongly on the products of transition dipole matrix elements in the numerators. It is then possible to find initial states Φ_1 and Φ_2 such that the interference contribution is large enough to significantly alter the deposition pattern.

This qualitative argument has been confirmed by extensive numerical studies. Among the states studied, we found that the 7s + 7d superposition state is the most suitable, and deposition results for this superposition state are presented below. In all cases, the field intensities were chosen to be $E_1^{(0)} = E_2^{(0)} = 3.16$ W/cm^2 and the detuning from the 10p level to be 1 MHz. The wavelengths of the two fields were $\lambda_1 = 1.88$ μm and $\lambda_2 = 7.17$ μm.

The size of the Rb beam is 15 μm, chosen in accord with the requirement $-a\lambda_2 \le x \le a\lambda_2$ with $a = 1$. The size of the segment of the substrate where the deposited density is calculated is 2.5 times larger than the atomic beam size, large enough to encompass the entire deposition region. Note that conventional experiments produce atomic beams whose diameter ranges from 5 to 100 μm. If we were to use a Rb beam that is bigger than 15 μm, then the entire deposition pattern would be a periodic repetition of the sub-region pattern formed by the 15 μm beam.

Both the system and initial state are chosen to avoid a number of loss mechanisms. Consider first the issue of spontaneous emission. Rydberg atoms have relatively long radiative lifetimes τ due to their small dipole coupling to the ground state and other low-lying states. For example, in the 7s state $\tau \approx 90$ ns.[42,53] To minimize spontaneous emission losses, the interaction time is chosen so that $t_{inter} < \tau$, with the former being controlled by changing the laser's waist or the atoms' longitudinal velocity. Typically (except for the results in Figures 3 and 9), $t_{inter} = 25$ ns.

A second loss mechanism of concern is ionization, since Rydberg atoms are easily ionized. Ionization may present a problem during laser focusing because it alters the optical potential felt by the atom, degrading the resolution of the deposition pattern. Hence, we employ relatively weak focusing fields to avoid ionization. The field necessary to ionize a given Rydberg state is $E_{ion} = 1/(16n^{*4})$ (a.u.).[44] For the superposition state considered in this paper $n^* = 5.67$ so that the maximum field intensity we can allow is 3×10^7 V/m. The electric fields used below are of maximum intensity 10^6 V/m, well below this limit.

Also of concern are stray electric fields. In our coherent control simulations, the smallest electric field is 5×10^3 V/m. A typical stray electric field of 10 mV/cm would induce a potential that is 2.5×10^7 times smaller than the LIP and would not affect the formation of the deposition patterns. It can, however, modify the composition of the initial 7s + 7d superposition state if weak fields are used to prepare that state. Such a change in the amplitude ratio $|b_1/b_2|$ will affect the brightness of the deposition patterns (see the discussion regarding Figure 8).

Note that in our coherent control scenario the Rydberg atoms are in a state of relatively low principal quantum number ($n = 7$). In case of high principal quantun numbers ($n > 20$), the lower limit on the field strength imposed by the ionization will make the deposition patterns much more sensitive to the stray fields.

Figure 4 shows the total light-induced potential and the interference-induced and non-interference contributions, as well as the resultant deposition pattern. As in the periodic case of Figure 3, the minima of the LIP serve as focusing centers and the maxima as defocusing centers. Figure 3a shows that the potential wells associated with $V^{non}(x)$ are separated by $\approx \lambda_2/2$. The $V^{int}(x)$ contribution is, however, aperiodic, containing minima of variable depth and position. In addition, these potential wells are steeper that those of $V^{non}(x)$, resulting in a larger dipole force. Due to the aperiodic characteristic of the interference-induced potential, the total LIP is also aperiodic, leading to an aperiodic deposition pattern. Further note that, although the interference-induced contribution contains repulsive parts, the total LIP is attractive. (Note that the captions provide the parameters used for the computations shown in the figures.)

To more clearly assess the role of the atomic coherence we show, in Figure 5, the LIP and deposition pattern associated

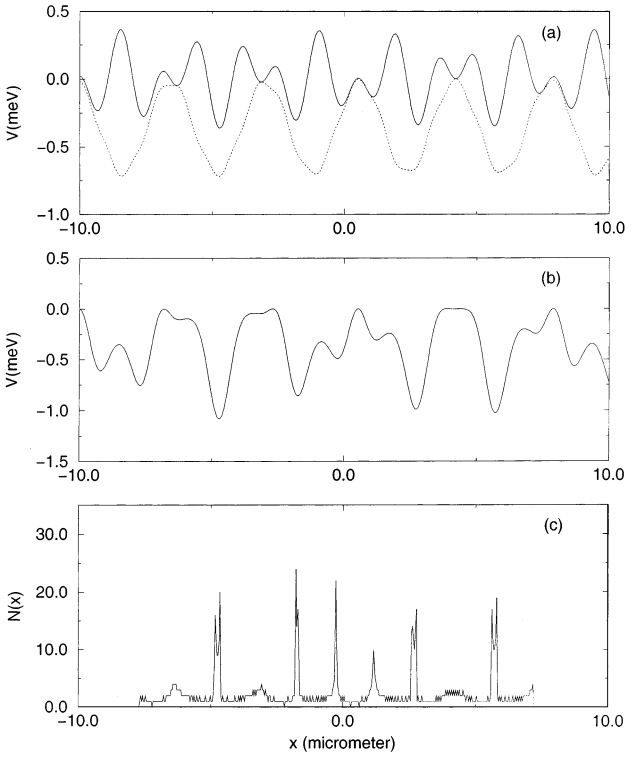

Figure 4. (a) Contributions to the light-induced potential: $V^{non}(x)$ (dotted line) and $V^{int}(x)$ (full line); (b) the total light-induced potential $V(x) = V^{non}(x) + V^{int}(x)$; and (c) the deposition pattern for the $\sqrt{0.8}|\ 7,\ 0,\ 0\rangle + \sqrt{0.2}|7,\ 2,\ 0\rangle$ superposition state. The size of the beam and plate is 15 μm. A total of 1000 atomic trajectories have been used, with the transverse velocity taken as zero. The field intensity is 3.16 W/cm^2. Other parameters are: $\phi_M = 0$, $\phi_F = (\pi/3)$, $t_{inter} = 0.025$ μs, $\lambda_1 = 1.88$ μm, and $\lambda_2 = 7.17$ μm. Here and below all angles are in radians.

with the $V^{non}(x)$ contribution to the potential shown in Figure 4. The results show a pattern composed of much weaker and broader peaks, spaced $\approx \lambda_2/2$ apart, superimposed on a significant background. Note that the average potential depth of $V^{non}(x)$ is ≈ 0.75 meV, which is of the same order of magnitude as the total LIP ($\approx$1.0 meV). Thus the broadening of the deposited peaks is not caused by the small decrease in the depth of the minima, but rather due to a change in the shape of the LIP. Thus, in addition to introducing aperiodicities in the deposition patterns, V^{int} plays an important role in sharpening the deposition pattern. Specifically, a comparison of the peaks in Figures 5 and 4 show that the introduction of the interference contribution narrows the peaks by a factor of 3 and increases the contrast with the background by a factor of 5.

The coherent control approach provides for control through a wide variety of experimentally adjustable control parameters. Consider first ϕ_M, the relative phase between b_1 and b_2. This term affects $V^{int}(x)$, which depends on ϕ_M through $b_1 b_2^*$ and $b_1^* b_2$ [eq 27]. The phase ϕ_M alters relative contributions of the interference-induced and non-interference contributions, resulting in different total LIPs and different deposition patterns. This is demonstrated numerically in Figure 6, where the deposition patterns for a fixed $\phi_F = (\pi/3)$, and variable $\phi_M = 0$ in (b), $(\pi/3)$ in (d), and π in (f) are shown. The number of deposited peaks varies from six in panel (b) to four in panel (d) and nine in (f). It is evident that the positions, number, and the heights of the peaks are very sensitive to changes in ϕ_M. For example in panel (b), in the central region of the plate (from -3 to 3 μm) the deposition peaks are separated by $\approx \lambda_1$, whereas they are separated by $\lambda_2/2$ in the same region in panel (d). Because

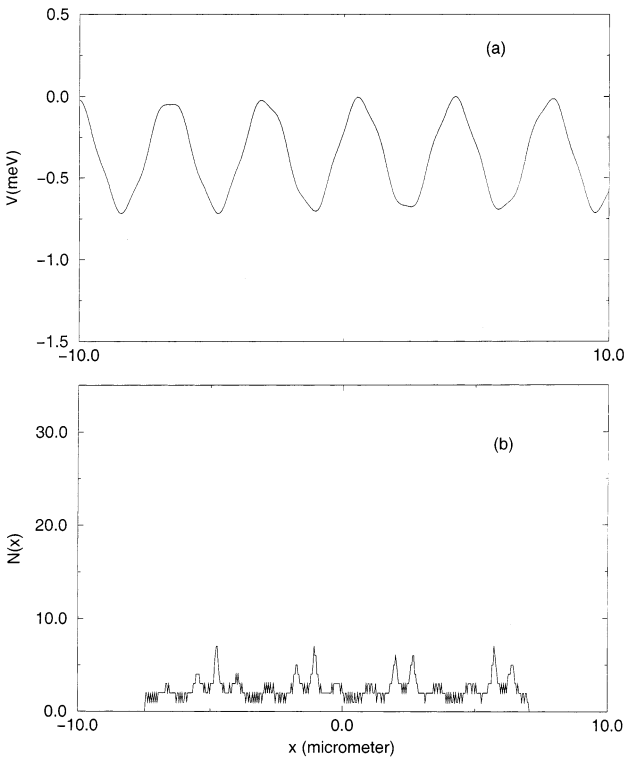

Figure 5. Same as in Figure 4. (a) The noninterference potential, $V^{non}(x)$, and (b) the resulting deposition pattern.

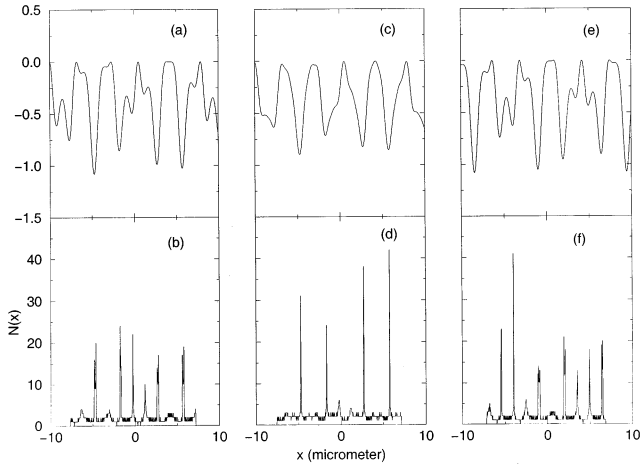

Figure 6. Panels (a), (c), and (e): LIP and deposition patterns (panels b, d, f) associated with the $\sqrt{0.8}|\ 7,\ 0,\ 0\rangle + \sqrt{0.2}|7,\ 2,\ 0\rangle$ superposition state. $\phi_F = (\pi/3)$ and $\phi_M = 0$ in (a,b), $(\pi/3)$ in (c,d), and π in (e,f).

ϕ_F is fixed, the $V^{non}(x)$ contribution to LIP is unchanged. Therefore, the variation in the total LIPs shown in (a), (c), and (e) results from the changes in $V^{int}(x)$.

A second control parameter is ϕ_F, the relative phase between the two laser fields. Figure 7 shows the deposition patterns for a fixed $\phi_M = 0$, at $\phi_F = 0$ in (b), $(\pi/3)$ in (d), and π in (f). We observe from the figure that there are five significant peaks in (b), six in (d), and six in (f). As compared to ϕ_M, the number of the peaks depends less sensitively on ϕ_F, but changing ϕ_F allows one to manipulate the location of the minima and maxima, i.e., the focusing and defocusing centers, of the total LIP, as shown in panels (a), (c), and (e).

In addition to ϕ_M, the initial superposition state depends on the amplitude ratio $|b_1/b_2|$ which can be altered experimentally by changing the pulse parameters in the preparation step of the superposition state. Figure 8 shows the dependence of the

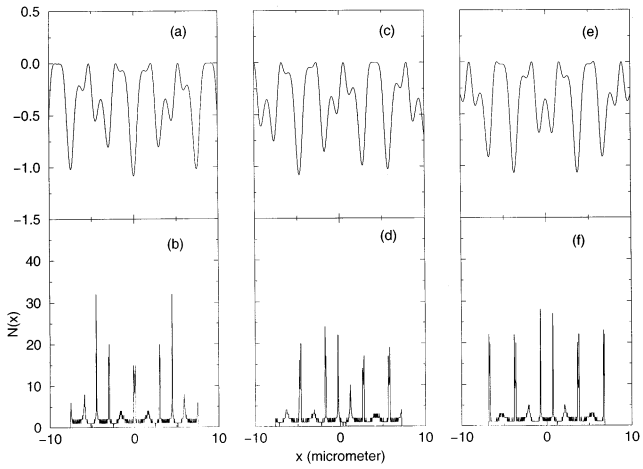

Figure 7. LIP (panels a,c,e) and deposition patterns (panels b,d,f) associated with the $\sqrt{0.8}|7, 0, 0\rangle + \sqrt{0.2}|7, 2, 0\rangle$ superposition state. $\phi_M = 0$ and $\phi_F = 0$ in (a,b), $(\pi/3)$ in (c,d), and π in (e,f).

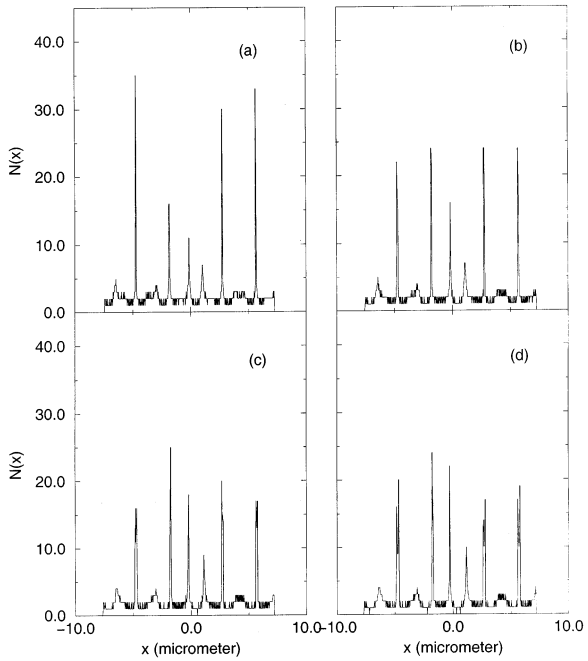

Figure 8. Deposition patterns associated with the $b_1|7, 0, 0\rangle + b_2|7, 2, 0\rangle$ superposition state. $|b_2|^2 = 0.05$ in panel (a), 0.1 in (b), 0.15 in (c), and 0.2 in (d). Other parameters are $\phi_M = 0$, $\phi_F = (\pi/3)$.

deposition on $|b_2|$, where $|b_2|^2 < 0.2$, consistent with preparation via perturbation theory. Note that changing $|b_2|$ does not affect the location of the peaks. It does, however, modify the height of the peaks, altering the brightness of the deposited pattern.

In addition to these control parameters arising from the coherent control scenario, there are other traditional control parameters that originate from the particular experimental setup in nanolithography. Specifically one can alter t_{inter}, the time of interaction of the atoms with the light source, and L_{ff}, the free-flight distance during which the atoms travel after having interacted with the laser and before colliding with the surface. Because of the deleterious effects of the transverse velocity, increasing the free-flight distance generally degrades the sharpness of the deposition pattern; in our case $L_{\text{ff}} = 0$. Similarly, t_{inter}, the interaction time (which must be less than the lifetime of the Rydberg state), has a direct effect on the resolution of the deposition pattern. Figure 9 shows the result for different interaction times. Note that when t_{inter} is small (e.g., Figure 9a), the atoms do not have enough time to be influenced by the LIP,

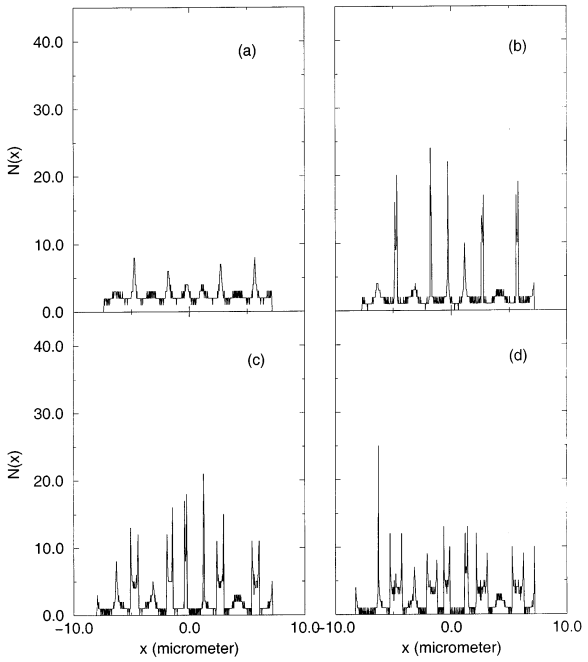

Figure 9. Deposition patterns associated with the $\sqrt{0.8}|7, 0, 0\rangle + \sqrt{0.2}|7, 2, 0\rangle$ superposition state. $t_{\text{inter}} = 0.015$ μs in (a), 0.025 μs in (b), 0.035 μs in (c), and 0.045 μs in (d). Other parameters are $\phi_M = 0$, $\phi_F = (\pi/3)$.

and focusing cannot be achieved. On the other hand if t_{inter} is too long, the optical force deflects the atoms more than it should, causing broadening and splitting of the peaks (Figure 9c and d). Among the examples shown, the best interaction time is 0.025 μs (Figure 9b). Note that in case of atoms in a single state interacting with one laser field, it is possible to derive an analytic expression giving the optimal t_{inter} that gives the best focusing.[54] In our case, however, the atoms are prepared in a superposition state, and the total LIP consists of potential wells of various depth with aperiodic spacing. One cannot therefore determine the optimal t_{inter} analytically. However, it can be obtained by using an optimal control scenario.

Our coherent control results have assumed a perfectly collimated atomic beam. To account for a less-than-ideal situation requires that we include the transverse velocity distribution. Theoretically, the transverse kinetic energy of the atom must be smaller than the depth of the potential well in order to ensure no escape from the well. This condition gives the maximum allowed transverse velocity $v_{\perp}^{\max} = \sqrt{2|V_{\text{LIP}}^{\max}|/M}$. This $v_{\perp}^{\max}$ is a function of the atom eigenstate, the light intensity, and frequency. In our examples, the average depth of the potential is ~ 0.5 meV, from which a maximum allowed transverse velocity of 34 m/s can be derived. However, computer simulation has shown that even a small transverse velocity of about 5 m/s can broaden the peaks considerably. The broadening is due to the fact that atoms with transverse velocities can gain bigger transverse momentum and hence leave the focus. One way to counter this problem is to optimize the control parameters so as to reduce the damage caused by the transverse velocity.[57] Chromatic aberration resulting from the longitudinal velocity spread has less degrading effect on the line width. Indeed, including a velocity spread as large as $\delta v_{\parallel}/v_{\parallel} \approx 1$ would broaden the line width by 36% with respect to that obtained with a monochromatic beam.[58]

In our numerical simulations, the atoms were treated as point-like particles and their center-of-mass motion calculated according to the laws of classical mechanics. In reality, the size

of the Rydberg atom, which is equal to n^2a_0, must be taken into account. Thus, the 10s state is 5.9 nm, whereas that of a 100s state atom is 5900 nm. The atom's unusually large size would decrease the resolution of the deposition were it to remain in the Rydberg state after striking the surface. Fortunately, the weakly bound Rydberg electron undergoes tunneling ionization[55,56] as the atom approaches to within $\approx 3.7n^2a_0$ of the surface. The remaining ion is then neutralized on the surface by an Auger process. Hence we expect that the ionization process will reduce the size of the Rydberg atom to that of the ground-state atom, preventing the degradation of the resolution of the deposited line. In our model the distance between the nozzle and the plate is 12.5 μm, and the distance at which the ionization occurs is ≈ 0.04 μm. Hence tunneling ionization does not degrade the deposition pattern. However, once the atoms are deposited on the surface, growth and diffusion phenomena can broaden the line width by 20−30 nm and reduce the contrast to ≈1:1.[59] One solution is to optimize the experimental parameters in the standing wave fields and the atomic beam. A control scenario for surface diffusion would also be useful.

Finally, we note that despite the improvement in line width due to the introduction of the interference contribution, the resultant lines are still relatively broad, with widths on the order of 50 nm. This width results from the fact that we have chosen to focus on producing aperiodic sets of lines via a scenario that allows for control over the line pattern by manipulating the laser parameters, and to do so with Rydberg atoms that allow for weak fields, using a fixed distance between the source and the surface. No explicit focus was placed on narrowing the deposition lines. However, as the discussion in this paper made clear, there are a wide variety of system parameters that can be varied in order to target alternative features, such as narrow deposition lines. Under these circumstances, given the large number of possible system parameters, the best approach is to design an optimization scheme to reach specific targets. This is discussed in a future paper,[57] where we demonstrate that, for example, one can optimize to produce a single Rb peak as narrow as one nanometer in width.

V. Summary

In this paper we have shown that bichromatic control of Rydberg atoms in superposition states provides a means of producing controllable aperiodic deposition patterns on surfaces that can be manipulated by changing the constitution of the initial superposition state and the phase between the two incident light fields. Other control parameters, such as the interaction time, were also shown to modify the resulting pattern. Although the creation of a completely arbitrary pattern is still in the future, it is clear that coherent control offers useful flexibility in fabricating nanoscale patterns. Explorations of producing arbitrary patterns using multicolored optimal and coherent control methodologies are underway.[57]

Acknowledgment. PB and MS acknowledge the longstanding personal support, interest, and contributions of Professor Richard Bersohn to their lives. Richard was a shining example of personal integrity and scientific commitment. He will be sorely missed. We thank the U.S. Office of Naval Research for support and H. R. Sadeghpour (Harvard) for suggesting that we treat Rydberg atoms.

References and Notes

(1) For a review see, Ito, T.; Okazaki, S. *Nature* **2000**, *406*, 1027.

(2) Bell, A. S.; Pfau, T.; Drodofsky, U.; Stuhler, J.; Schulze, T.; Brezger, B.; Nowak, S.; Mlynek, J. *Microelectron. Eng.* **1998**, *42*, 587.

(3) Lison, F.; Adams, H. J.; Haubrich, D.; Kreis, M.; Nowak, S.; Meschede, D. *Appl. Phys. B* **1997**, *65*, 419.

(4) Berggren, K. K.; Younkin, R.; Cheung, E.; Prentiss, M.; Black, A. J.; Whitesides, G. M.; Ralph, D. C.; Black, C. T.; Tinkham, M. *Adv. Mater.* **1997**, *9*, 52.

(5) Thywissen, J. H.; Johnson, K. S.; Younkin, R.; Dekker, N. H.; Berggren, K. K.; Chu, A. P.; Prentiss, M.; Lee, S. A. *J. Vac. Sci. Technol.* **1997**, *B15*, 2093.

(6) Bell, A. S.; Brezger, B.; Drodofsky, U.; Nowak, S.; Pfau, T.; Stuhler, J.; Schulze, T.; Mlynek, J. *Surf. Sci.* **1999**, *435*, 40.

(7) Bradley, C. C.; Anderson, W. R.; McClelland, J. J.; Celotta, R. J. *Appl. Surf. Sci.* **1999**, *141*, 210.

(8) McClelland, J. J.; Celotta, R. J. *Thin Solid Films* **2000**, *367*, 25.

(9) Timp, G.; Behringer, R. E.; Tennant, D. M.; Cunningham, J. E.; Prentiss, M.; Berggren, K. K. *Phys. Rev. Lett.* **1992**, *69*, 1636.

(10) Drodofsky, U.; Drewsen, M.; Pfau, T.; Nowak, S.; Mlynek, J. *Microelectron. Eng.* **1996**, *30*, 383.

(11) Bjorkholm, J. E.; Freeman, R. R.; Ashkin, A.; Pearson, D. B. *Phys. Rev. Lett.* **1978**, *41*, 1361.

(12) Sleator, T.; Pfau, T.; Balykin, V.; Mlynek, J. *Appl. Phys.* **1992**, *B54*, 375.

(13) Prentiss, M.; Timp, G.; Bigelow, N.; Behringer, R. E.; Cunningham, J. E. *Appl. Phys. Lett.* **1992**, *60*, 1027.

(14) McClelland, J. J.; Scholten, R. E.; Palm, E. C.; Celotta, R. J. *Science* **1993**, *262*, 877.

(15) McGowan, R. W.; Giltner, D. M.; Lee, S. A. *Opt. Lett.* **1995**, *20*, 2535.

(16) Cook, R. J.; Hill, R. K. *Opt. Commun.* **1982**, *43*, 258.

(17) Balykin, V. I.; Letokhov, V. S.; Ovchinnikov, B. Yu.; Sidorov, A. I. *Phys. Rev. Lett.* **1988**, *60*, 2137.

(18) Aminoff, C. G.; Steane, A. M.; Bouyer, P.; Desbiolles, P.; Dalibard, J.; Cohen-Tannoudji, C. *Phys. Rev. Lett.* **1993**, *71*, 3083.

(19) Kasevich, M. A.; Weiss, D. S.; Chu, S. *Opt. Lett.* **1990**, *15*, 607.

(20) Kasevich, M. A.; Chu, S. *Phys. Rev. Lett.* **1991**, *67*, 181.

(21) Gould, P. L.; Ruff, G. A.; Pritchard, D. E. *Phys. Rev. Lett.* **1986**, *56*, 827.

(22) Lawall, J.; Prentiss, M. *Phys. Rev. Lett.* **1994**, *72*, 993.

(23) Renn, M. J.; Montgomery, D.; Vdovin, O.; Anderson, D. Z.; Wieman, C. E.; Cornell, E. A. *Phys. Rev. Lett.* **1995**, *75*, 3253.

(24) Ito, H.; Nakata, T.; Sakaki, K.; Ohtsu, M.; Lee, K. I.; Jhe, W. *Phys. Rev. Lett.* **1996**, *76*, 4500.

(25) Metcalf, H.; van der Straten, P. *Phys. Rep.* **1994**, *244*, 203.

(26) Askar'yan, G. A. *Sov. Phys. JETP* **1962**, *15*, 1088.

(27) Letokhov, V. S. *JETP Lett.* **1968**, *7*, 272.

(28) Ashkin, A. *Phys. Rev. Lett.* **1970**, *24*, 156.

(29) Ashkin, A. *Phys. Rev. Lett.* **1978**, *40*, 729.

(30) Chu, S.; Bjorkholm, J. E.; Ashkin, A.; Cable, A. *Phys. Rev. Lett.* **1986**, *57*, 314.

(31) Adams, C. S.; Sigel, M.; Mlynek, J. *Phys. Rep.* **1994**, *240*, 143.

(32) Chu, S. *Rev. Mod. Phys.* **1998**, *70*, 686.

(33) Seideman, T. *J. Chem. Phys.* **1997**, *106*, 2881.

(34) Seideman, T. *Phys. Rev. A* **1997**, *56*, R17.

(35) Gordon, R. J.; Zhu, L.; Schroeder, W. A.; Seideman, T. *J. Appl. Phys.* **2003**, *94*, 669.

(36) DeMarco, B.; Jin, D. S. *Phys. Rev. A* **1998**, *58*, R4267.

(37) Brumer, P.; Shapiro, M. *Faraday Discuss. Chem. Soc.* **1986**, *82*, 177. Shapiro, M.; Brumer, P. *Adv. Atom. Mol. Opt. Phys.* **2000**, *42*, 287.

(38) Rice, S. A.; Zhao, M. *Optical Control of Molecular Dynamics*; John Wiley & Sons: New York, 2000.

(39) Shapiro, M.; Brumer, P. *Principles of the Quantum Control of Molecular Processes*; John Wiley & Sons: New York, 2003.

(40) McCullough, E.; Shapiro, M.; Brumer, P. *Phys. Rev. A* **2000**, *61*, 041801(R).

(41) Dey, B.; Shapiro, M.; Brumer, P. *Phys. Rev. Lett.* **2000**, *85*, 3125.

(42) Gounand, F. *J. Phys. (Paris)* **1979**, *40*, 457.

(43) Nguyen, N. A.; Shapiro, M.; Brumer, P., work in progress.

(44) Gallagher, T. F. *Rydberg Atoms*; Cambridge University Press: Cambridge, 1994.

(45) Nez, F.; Plimmer, M. D.; Bourzeix, S.; Julien, L.; Biraben, F.; Felder, R.; Acef, O.; Jondy, J. J.; Laurent, P.; Clairon, A.; Abed, M.; Millerioux, Y.; Juncar, P. *Phys. Rev. Lett.* **1992**, *69*, 2326.

(46) Lebedev, V. S. *Physics of Highly Excited Atoms and Ions*; Springer-Verlag: New York, 1998.

(47) Kostelecky, V. A.; Nieto, M. M. *Phys. Rev. A* **1985**, *32*, 3243.

(48) O'Sullivan, M. S.; Stoicheff, B. P. *Phys. Rev. A* **1985**, *31*, 2718.

(49) Procter, S. R.; Yamakita, Y.; Merkt, F.; Softley, T. P. *Chem. Phys. Lett.* **2003**, *374*, 667.

(50) Ramsey, N. *Molecular Beams*; Clarendon: Oxford, 1956.

(51) Sheehy, B.; Shang, S.-Q.; van der Straten, P.; Metcalf, H. *Chem. Phys.* **1990**, *145*, 317.

(52) Gould, P. L.; Ruff, G. A.; Martin, P. J.; Pritchard, D. E. *Phys. Rev. A* **1987**, *36*, 1478.
(53) Theodosiou, C. E. *Phys. Rev. A* **1984**, *30*, 2881.
(54) Berggren, K. K.; Prentiss, M.; Timp, G. L.; Behringer, R. E. *J. Opt. Soc. Am. B* **1994**, *11*, 1166.
(55) Burgdörfer, J.; Lerner, P.; Meyer, F. W. *Phys. Rev. A* **1991**, *44*, 5674.
(56) Hill, S. B.; Haich, C. B.; Zhou, Z.; Nordlander, P.; Dunning, F. B. *Phys. Rev. Lett.* **2000**, *85*, 5444.
(57) Nguyen, N. A.; Shapiro, M.; Brumer, P., submitted.
(58) McClelland, J. J. *J. Opt. Soc. Am. B* **1995**, *12*, 1761.
(59) Behringer, R. E.; Natarajan, V.; Timp, G. *Appl. Surf. Sci.* **1996**, *104*, 291.